HHS Public Access

Author manuscript

Nano Lett. Author manuscript; available in PMC 2022 May 16.

Published in final edited form as:

Nano Lett. 2020 October 14; 20(10): 7159–7167. doi:10.1021/acs.nanolett.0c02487.

Targeted Radiosensitizers for MR-Guided Radiation Therapy of Prostate Cancer

Dong Luo,
Department of Radiology, Case Western Reserve University, Cleveland, Ohio 44106, United States

Andrew Johnson,
Department of Chemistry, Molecular Biosciences, Neurobiology, and Radiology, Northwestern University, Evanston, Illinois 60208, United States

Xinning Wang,
Department of Biomedical Engineering, Case Western Reserve University, Cleveland, Ohio 44106, United States

Hao Li,
Department of Chemistry, Molecular Biosciences, Neurobiology, and Radiology, Northwestern University, Evanston, Illinois 60208, United States

Bernadette O. Erokwu,
Department of Radiology, Case Western Reserve University, Cleveland, Ohio 44106, United States

Sarah Springer,
Department of Chemistry, Case Western Reserve University, Cleveland, Ohio 44106, United States

Jason Lou,
Department of Chemistry, Case Western Reserve University, Cleveland, Ohio 44106, United States

Gopalakrishnan Ramamurthy,
Department of Radiology, Case Western Reserve University, Cleveland, Ohio 44106, United States

Chris A. Flask,

Corresponding Authors: **Thomas J. Meade** – *Department of Chemistry, Molecular Biosciences, Neurobiology, and Radiology, Northwestern University, Evanston, Illinois 60208, United States*; tmeade@northwestern.edu; **James P. Basilion** – *Department of Radiology and Department of Biomedical Engineering, Case Western Reserve University, Cleveland, Ohio 44106, United States*; jxb206@case.edu.

Author Contributions

D.L., J.B., C.B., and T.M. designed this study, conducted experiments, and drafted the manuscript. A.J. and H.L. synthesized the Gd(III) and Y(III) complexes. X.W. gave directions on experiments design. S.S. and J.L. participated in peptides synthesis and cell studies. G.R. assisted on the tumor models and the biological analysis of the molecular target. B.E. and C.F. helped with MR scanning and sequence optimization. The manuscript was written through contributions of all authors. All authors have given approval to the final version of the manuscript.

The authors declare the following competing financial interest(s): J.B. and X.W. hold stock in Exotome LLC, a company that holds the comercialization license for the PSMA ligand used in these studies. All other authors declare no competing financial interest.

Department of Radiology and Department of Pediatrics, Case Western Reserve University, Cleveland, Ohio 44106, United States

Clemens Burda,
Department of Chemistry, Case Western Reserve University, Cleveland, Ohio 44106, United States

Thomas J. Meade,
Department of Chemistry, Molecular Biosciences, Neurobiology, and Radiology, Northwestern University, Evanston, Illinois 60208, United States

James P. Basilion
Department of Radiology and Department of Biomedical Engineering, Case Western Reserve University, Cleveland, Ohio 44106, United States

Abstract

Adjuvant radiotherapy is frequently prescribed to treat cancer. To minimize radiation-related damage to healthy tissue, it requires high precision in tumor localization and radiation dose delivery. This can be achieved by MR guidance and targeted amplification of radiation dose selectively to tumors by using radiosensitizers. Here, we demonstrate prostate cancer-targeted gold nanoparticles (AuNPs) for MR-guided radiotherapy to improve the targeting precision and efficacy. By conjugating Gd(III) complexes and prostate-specific membrane antigen (PSMA) targeting ligands to AuNP surfaces, we found enhanced uptake of AuNPs by PSMA-expressing cancer cells with excellent MR contrast and radiation therapy outcome *in vitro* and *in vivo.* The AuNPs binding affinity and r_1 relaxivity were dramatically improved and the combination of Au and Gd(III)provided better tumor suppression after radiation. The precise tumor localization by MR and selective tumor targeting of the PSMA-1-targeted AuNPs could enable precise radiotherapy, reduction in irradiating dose, and minimization of healthy tissue damage.

Graphical Abstract

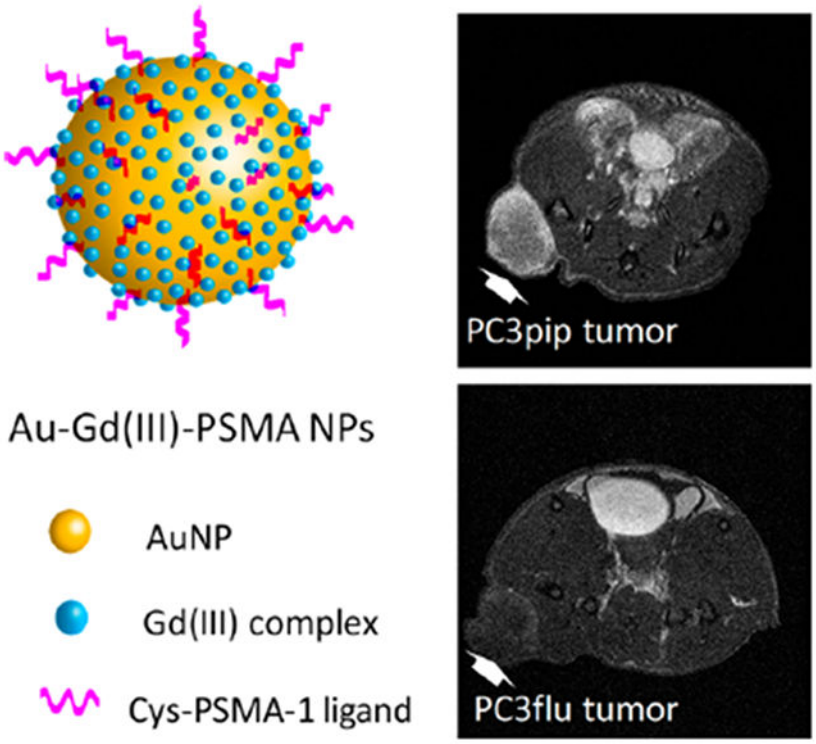

Keywords

Radiosensitizer; nanoparticles; MR-guided radiotherapy; PSMA targeting; prostate cancer

Radiotherapy is prescribed for more than 50% of prostate cancer patients.[1,2] Adjuvant radiation has been shown to mitigate disease progression in randomized phase III trials for men with high risk features such as seminal vesicle involvement, extra-capsular extension, or positive margins.[3–5] Development of radiation technology, such as utilizing intensity-modulated radiotherapy (IMRT) which delivers highly conformal radiation dose distributions and image-guided radiotherapy (IGRT) that accounts for daily changes in target anatomy and positioning, allows unprecedented levels of accuracy and therapy outcome.[6–10] However, because the prostate is surrounded by many essential nerves and muscle fibers, it still remains a challenge to precisely localize and deliver proper radiation doses to tumors without untoward effects resulting.

Magnetic resonance imaging (MRI) is a powerful clinical imaging modality that provides high-resolution three-dimensional images of soft tissues[11–13] and is being applied to prostate cancer diagnosis.[14] Magnetic resonance (MR) molecular imaging of prostate cancer biomarkers can facilitate noninvasive prostate cancer detection and image-guided therapy.[8,15–18] MR-guided radiotherapy (RT) is considered an important component for the future of radiotherapy.[19] Adverse effects of RT can be mitigated by employing radiosensitizers that locally enhance the radiotherapeutic effect.[20,21] Nanoparticle sensitizers allow for better targeting precision and lower radiation doses to the surrounding normal tissues, when properly employed,[20,21] and can provide a means for further relative biological

dose escalation sparing normal tissue.[22,23] So far, there has been limited preclinical and clinical investigation of targeted radiosensitizers for prostate cancer.[24] Therefore, there remains an unmet clinical need to improve imaging for identifying cancerous prostate tissue followed by radiotherapy without damaging surrounding tissues. Here, we present a nanoparticle-based radiosensitizer that will improve prostate cancer tissue visualization and discrimination by MRI allowing for greater accuracy and efficacy during image-guided RT.

Gold nanoparticles (AuNPs) are the next generation of radiosensitizers for radiotherapy,[25] and actively targeted AuNPs can selectively enhance radiation doses to targeted diseased tissues and minimize off-target tissue damage. Recently, we have synthesized a new high-affinity ligand to prostate-specific membrane antigen (PSMA), which is overexpressed in prostate cancer.[26,27] We have demonstrated that the PSMA-targeted AuNPs can be used to increase the efficacy of radiation doses to prostate cancer.[28] Some recent studies have demonstrated using nanoparticles as MR contrast agents and radiosensitizers for MR-guided radiation therapy in animals.[29–33] However, all of them are untargeted and delivered via an enhanced permeability and retention (EPR) effect, which limits the selectivity and deposition into tumors.

In this study, we synthesized PSMA-targeted AuNPs to selectively deliver Gd(III) contrast agents to prostate cancer, resulting in contrast enhanced MRI. Radiation after NP injection significantly inhibited tumor growth, and diffusion-weighted imaging revealed tumor response to the Au–Gd(III)-PSMA NP-enhanced radiotherapy.

RESULTS AND DISCUSSION

The Au–Gd(III)-PSMA NPs were synthesized by conjugating Gd(III) complex to the AuNP surface, and active targeting of the Au–Gd(III)NPs was achieved by grafting Cys-PSMA-1 ligands, as shown in Figure 1a. The Gd(III) complex was synthesized with minor modifications of our previously reported protocol.[34] To verify the radiosensitizing effect of Gd(III), an analogous complex was synthesized with yttrium, Y(III). The details are provided in the Supporting Information (Figures S1–S3). The 1,2-dithiolane anchor with cyclic disulfide functionality has shown excellent surface binding affinity for gold, which binds the Gd(III) or Y(III) complex firmly to the AuNP surface.[35] Moreover, the lipoic acid sequence of the Gd(III) complex improves the colloidal stability of our AuNPs,[36] allowing us to eliminate the need for PEGylation as a particle stabilizer and retaining the small size of the Au–Gd(III)-PSMA NPs. TEM revealed that the Au–Gd(III)-PSMA NPs have a narrow core size distribution and an average diameter of 5 nm (Figure 1b), and after conjugating Cys-PSMA-1 ligands, the hydrodynamic (HD) diameter was 7.8 nm (Figure 1c). The stability of NPs in serum was monitored by gel electrophoresis, as described previously.[37,38] After incubating with 10% fetal bovine serum (FBS), a clear separation between the FBS band and the Au–Gd(III)-PSMA NPs band was observed, indicating limited irreversible

Supporting Information

The Supporting Information is available free of charge at https://pubs.acs.org/doi/10.1021/acs.nanolett.0c02487.

Experimental section, synthesis and characterization of Gd(III) and Y(III) complexes, PSMA ligand, functionalization of the Au–Gd(III)-PSMA NPs, stability and relaxivity measurements, MR imaging of Au–Gd(III)-PSMA NPs solutions, ICP measurment of NPs *in vivo* distributions, and ADC maps of mice before and after NPs injection (PDF)

serum adsorption to the particle surface (Figure 1d). An increased mobility of the targeted AuNP toward the anode suggests the successful conjugation of Cys-PSMA-1 to AuNP, as PSMA-1 has a negative charge. The UV–vis absorbance of the NPs tested in PBS (pH at 5.5 and 6.5) or serum over time confirmed long-term neutral and acidic stability (Figure S4).

Table 1 shows the relaxivities, where the untargeted Au–Gd(III)NPs have an r_1 of 32.3 mM^{-1} s^{-1} at 37 °C (1.4 T), with a total surface loading of 258 ± 63 Gd(III) complexes per particle, and the Au–Gd(III)-PSMA NPs have an r_1 = 20.6 mM^{-1} s^{-1} at 37 °C (1.4 T), with a total surface loading of 230 ± 10 Gd(III) complexes per particle (Figure S5–S8, Tables S1–S3).

We tested the selectivity of Au–Gd(III)-PSMA NPs *in vitro* with both PSMA-positive PC3pip and PSMA-negative PC3flu cells. After coincubating with Au–Gd(III)-PSMA NPs for 24 h, the PC3pip cells showed greater uptake than the PC3flu cells (Figure 2a). PC3pip cells had almost a 3-fold higher Au uptake and 2.5-fold higher Gd(III) uptake than the PC3flu cells, indicating a PSMA receptor-mediated uptake of NPs. The binding affinity of Au–Gd(III)-PSMA NPs was determined by a competition binding assay. Au–Gd(III)-PSMA NPs, Cys-PSMA-1 alone, as well as the parent ligand ZJ24 were added to LNcap cell suspensions and incubated for 1 h at the presence of ^{3}H-labeled ZJ24. The radioactivity retained by cells after extensive washes showed a remarkably lower half maximal inhibitory concentration (IC_{50}) of 0.07 × 10^{-9} M for the Au–Gd(III)-PSMA NPs compared to 1.26 × 10^{-9} M for the Cys-PSMA-1 and 9.79 × 10^{-9} M for the ZJ24 (Figure 2b). The significant improvement of binding affinity for the NPs is likely due to the multivalent binding effect, since multiple Cys-PSMA-1 ligands were covalently conjugated to the surface of each NP.[39]

To verify that enhanced uptake of Au–Gd(III)-PSMA NPs would improve contrast in MR imaging, we harvested both the PC3pip and PC3flu cells after 24 h coincubation with NPs and pelleted them in capillary tubes. PC3pip cell pellets incubated with Au–Gd(III)-PSMA NPs showed a visible pink color, originating from the NPs, which was absent for the PC3flu cell pellet (Figure 2c). MR scanning at 7 T distinguished the PC3pip cells, showing an enhanced contrast in the T_1-weighted image (Figure 2c). From this image, the increased signal-to-noise ratio (ΔSNR) for PC3pip cells was calculated to be 3.3 which was significantly higher than 0.8 for the PC3flu cells (Figure 2d). Clinical Gd(III)-based MRI contrast agents are usually not effectively internalized by cells.[40] Conjugating Gd(III) contrast agents to targeted-NPs enhances the uptake into cells and likely will further improve the specificity for MR imaging.

Since both Au and Gd(III) have a high Z number and a notable mass energy absorption coefficient over soft tissues, we investigated the combination of these atoms on radiation enhancement.[25,41] We synthesized AuNPs with yttrium (Y) complex bound to the surface as a negative control (Y has little mass energy absorption), and the chelated Gd(III) was replaced with Y(III) to ensure similar surface properties. First, we incubated PC3pip and PC3flu cells with various doses of Au–Gd(III)-PSMA NPs or Au–Y(III)-PSMA NPs for 24 h to evaluate the cytotoxicity. Neither of the NPs caused obvious toxicity to PC3pip or PC3flu cells with NP concentrations up to 50 nM (Figure 3a).

We hypothesized that an active NP uptake by PSMA targeting will sensitize cells to radiation, enhancing the radiation dose delivered to cells and leading to more effective cell killing. As confirmed by the survival fraction curves (Figure 3b), PC3pip cells incubated with Au–Gd(III)-PSMA NPs and irradiated showed a significantly lower survival rate compared to PC3flu cells or control cells at radiation doses above 2 Gy. Similar survival studies using Au–Y(III)-PSMA NPs (Figure 3c) showed that the radiation enhancement of Au–Y(III)-PSMA NPs was likely due to Au only. Compared to PC3pip cells incubated with Au–Gd(III)-PSMA NPs, PC3pip cells incubated with Au–Y(III)-PSMA NPs had a slightly higher survival rate. The sensitization enhancement ratios (SER, the ratio of survival fractions without and with NPs at a survival level of 50%) for PC3pip cells incubated with Au–Gd(III)-PSMA NPs and Au–Y(III)-PSMA NPs were calculated to be 1.7 and 1.5, respectively, trending toward an increase in radiation sensitivity due to Gd(III) but not differing significantly. Presumably, this is because the amount of Gd(III) conjugated to the AuNP surface is much lower than the Au content in the NPs and thus much less Gd(III) is internalized into the cells. The Au–Gd(III)-PSMA NPs and Au–Y(III)-PSMA NPs showed a high SER, at a much lower NP incubation concentration, compared to the other Au- or Gd(III)-based radiosensitizers,[42,43] likely owing to their excellent binding affinity to PC3pip cells.

To further demonstrate the selectivity of Au–Gd(III)-PSMA NPs to enhance killing of PSMA-expressing prostate cancer cells upon irradiation, we mixed equal amounts of NP-incubated PC3pip and PC3flu, irradiated the cell suspensions (4 Gy), and regrew them in 6-well plates to form colonies. Before imaging the mixed colonies, we incubated them with NPs again and stained them with silver[44] to distinguish the PC3pip and PC3flu colonies based on PSMA expression (Figure 3d). For the cell mixtures without radiation, we measured equal quantities of PC3pip (stained as black) and PC3flu (relatively transparent) colonies (Figure 3e), with a ratio of 1 (Figure 3f). In contrast, after irradiation, the PC3pip colony numbers were significantly reduced, with only a few black PC3pip colonies identifiable in the plate. There was little change in the number of PC3flu colonies. The PC3flu-to-PC3pip colony ratio increased to 8 after irradiation, suggesting that X-ray irradiation can selectively kill the PC3pip cells when Au–Gd(III)-PSMA NPs are internalized, even when they are very-well mixed with PC3flu cells. This selectivity feature is very important for clinical applications of radiation therapy since cancerous lesions are always adjacent to normal healthy tissues, underscoring that precisely targeted radiotherapy is urgently needed.

To evaluate the performance of Au–Gd(III)-PSMA NPs for prostate cancer imaging, animals were intravenously injected with Au–Gd(III)-PSMA NPs at 60 μmol Gd(III)/kg, which is about half of the standard dose for clinically used Gd(III)-DTPA and 1/5 of that for Gd(III)(HP-DO3A).[45] Significantly, increased contrast enhancement was observed for mice with PC3pip tumor for up to 24 h after NPs injection, peaking at approximately 6 h post-injection (Figure 4a). There was limited contrast enhancement for the PC3flu tumor over 24 h (Figure 4b). There was also dramatic MR signal in the bladder, indicating renal clearance of Au–Gd(III)-PSMA NPs due to their small size.[46] Quantitative analysis was done by subtracting the muscle signal from the tumor region of interest (ROI) and dividing by the standard deviation of the noise to generate the contrast-to-noise ratio (CNR) values.

Au–Gd(III)-PSMA NPs produced a dramatic CNR increase of 13.9 ± 0.8 for PC3pip tumors during the first 6 h post-injection (Figure 4c), while CNR for the PC3flu tumors did not increase significantly over time. The kinetics of CNR for PC3pip tumor has a similar trend to that of PSMA-targeted AuNPs accumulation in the tumors as revealed by CT scanning in our previous studies.[28,47] The small size of the Au–Gd(III)-PSMA NPs facilitates rapid tumor extravasation, selective tumor binding, and sustained MR contrast, which enabled prostate cancer detection with significantly improved sensitivity.

To further understand the performance observed in MR imaging, biodistribution of Au–Gd(III)-PSMA NPs was measured by ICP-MS at 24 h post-injection. Au and Gd(III) content in tumors and main organs were analyzed. As shown in Figure 4d, there was significantly more Au and Gd(III) accumulation in PC3pip tumors than in PC3flu tumors, about 3.6-fold and 2.6-fold more for Au and Gd(III), respectively. This supports our hypothesis that active targeting of the prostate tumor via the PSMA receptor facilitates better NP accumulation compared to untargeted uptake,[47] enhancing MR contrast in targeted tumors. The minimal enhancement in the PC3flu tumors likely is due to EPR. Since significant MR signal was observed in bladder, we collected the urine at 8 and 24 h post-injection, and the results of those collections showed that a large amount of Au and Gd(III) was detected in urine, especially at 8 h (about 2.1 μg Au and 0.6 μg Gd(III) per μL urine, Figure S9). The hydrodynamic diameter for NPs to get filtered by the glomerulus in the kidney is in the range of 6–8 nm and is dependent on their surface charge.[48] While our NPs can be excreted renally, many of them end up in the reticuloendothelial system (RES),[46] as a significant accumulation of Au–Gd(III)-PSMA NPs in the liver and spleen was observed (Figure S10), suggesting additional clearance pathways for the NPs via the RES and digestive systems.

To investigate the potential use of the Au–Gd(III)-PSMA NPs for radiotherapy of prostate cancer, mice bearing PC3pip tumor were injected with either Au–Gd(III)-PSMA NPs or Au–Y(III)-PSMA NPs, and radiation (6 Gy) was given once at 4 h or twice at both 4 and 48 h post-injection (Figure 5a).[28] Although the standard fractionation of 1.8–2.0 Gy per fraction and hypofractionation of 2.5–6.7 Gy per fraction are given to patients for radiotherapy of prostate cancer,[49] the radiation dose (6 Gy) was chosen here to see the best outcome and efficacy comparison of Au–Gd(III)-PSMA NPs and Au–Y(III)-PSMA NPs, since multiple radiation dosing was limited to 2 doses. Further, with improved tumor targeting and MR-guidance, the Au–Gd(III)-PSMA NPs have the potential for extreme hypofractionation applications in which 6–10 Gy per fraction is used for image-guided radiotherapy of prostate cancer.[50]

Mice injected with PBS and receiving the same treatment were used as controls. Tumor size and mouse body weight were then monitored for 30 days. In contrast to PBS control, both types of NPs resulted in obvious reduction in tumor growth (Figure 5b), suggesting enhancement of X-ray irradiation. Radiation enhancement was measured with NP doses increasing from 0.13 μmol NPs/kg (dash lines) to 0.26 μmol NPs/kg (solid lines) and was dose-dependent for both types of NPs. Comparing the growth curves of tumors receiving the two types of NPs, Au–Gd(III)-PSMA NPs had significantly better tumor inhibition than Au–Y(III)-PSMA NPs, suggesting complementatry radiosensitization by the combination of Au and Gd(III). However, giving only one irradiation at 4 h after NP injection did not

completely inhibit the prostate tumor growth and resulted in tumors growing back rapidly after 2 weeks. Therefore, we tested multiple X-ray irradiations, which is often performed in clinical radiotherapy of prostate cancer.[51]

At 48 h post NP injection we performed a second X-ray irradiation. In tumor-bearing mice injected with Au–Gd(III)-PSMA NPs, a second irradiation significantly reduced tumor growth, which only increased in size by 114% by day 30, compared to 300% for tumor-bearing mice injected with the same dose of NPs but receiving only one irradiation (Figure 5c). Body weight for all the mice receiving radiation did not show significant changes, indicating that the NPs were safe to use for radiotherapy. For mice without irradiation, the body weight dropped to 84% (Figure 5d), indicating progressing disease.

Apparent diffusion coefficient (ADC) is a direct reflection of water proton mobility. Since increased tumor necrosis can promote water molecule diffusion in tumors and result in enhanced (ADC) values,[52,53] we utilized diffusion-weighted imaging (DWI) to further evaluate tumor treatment outcome (Figure 5e). Alone the Au–Gd(III)-PSMA NP injection did not cause any changes to the ADC values (Figure S11), but after irradiation the ADC in the tumors was significantly increased 24 h after X-ray irradiation (Figure 5e). In contrast, irradiation alone without any NP injection did not cause any difference in ADC values. The changes of ADC value plotted in Figure 5f show that, with NP injection, irradiation increased the ADC significantly by 1.15×10^{-4} mm^2/sec after 24 h, whereas for the blank control, it increased marginally by 0.18×10^{-4} mm^2/sec. These DWI results suggest that the Au–Gd(III)-PSMA NP-enhanced radiotherapy for prostate cancer is based on destruction of the targeted cancer cells. This method could be used to monitor radiotherapy outcomes quantitatively and noninvasively during the radiotherapy.

In summary, we have described targeted Au–Gd(III)-PSMA NPs for prostate cancer MR imaging and radiotherapy. Both the Au and Gd(III) atoms can serve as radiosensitizers, and the conjugation of Gd(III) complexes onto AuNP surfaces improved MR sensitivity approximately 4-fold. The targeted Au–Gd(III)-PSMA NPs were prepared by conjugating Gd(III) complexes and a prostate-specific membrane antigen targeting ligand (Cys-PSMA-1) onto the AuNP surface. This surface modification increased the r_1 relaxivity by a factor of 4 *and* resulted in a higher binding affinity. The Au–Gd(III)-PSMA NPs have excellent selectivity to PSMA expressing prostate cancer cells and enhanced the MR contrast of cells and radiosensitization *in vitro.* Systemically administered Au–Gd(III)-PSMA NPs showed good tumor accumulation, MR contrast, and significant *in vivo* radiation dose amplification. With high prostate cancer targeting specificity, MR contrast sensitivity, and renal clearance, the Au–Gd(III)-PSMA NPs can inform future clinical MR-guided radiotherapy of prostate cancer. Ultimately, these particles may be used to lower the therapeutic X-ray dose by protecting normal surrounding tissue from radiation damage while allowing cancer cell destruction. Specifically, radiotherapy is advancing toward magnetic resonance linear accelerator (MR-LINAC) instrumentation. This combines a MRI scanner and linear accelerator to deliver radiation doses to the tumor more precisely for therapy of several different cancers, including prostate and pancreatic cancer.[54] The development of such a targeted MR imaging radiosensitizer may play a significant role in the development of MR-LINAC approaches. Significantly, PSMA receptor is overexpressed

in the neovasculature of most solid human tumors,[27] making the application of PSMA-targeted NP developed here to have a broader application for radiotherapy than just prostate cancer. The potential of PSMA as a vascular biomarker was highlighted by phase I trials that demonstrated specific targeting of tumor neovasculature by ^{111}In-labeled J591 in patients with kidney, colorectal, lung, bladder, pancreas, liver, breast and cancers and melanoma.[55] Studies of the Au–Gd(III)-PSMA NPs as a contrast agent and radiosensitizer for other solid tumors are under investigation.

Supplementary Material

Refer to Web version on PubMed Central for supplementary material.

ACKNOWLEDGMENTS

The authors gratefully acknowledge funding from the National Institutes of Health and the National Foundation for Cancer Research. The authors also thank John Mulvihill for the help with radiation experiments.

Funding

This research was supported by the National Institute of Health Grant, RO1 EB020353-03 and R01EB5866-6.

REFERENCES

(1). Hankey BF; Feuer EJ; Clegg LX; Hayes RB; Legler JM; Prorok PC; Ries LA; Merrill RM; Kaplan RS Cancer surveillance series: interpreting trends in prostate cancer–part I: Evidence of the effects of screening in recent prostate cancer incidence, mortality, and survival rates. J. Natl. Cancer Inst 1999, 91, 1017–1024. [PubMed: 10379964]

(2). Xie J; Gong L; Zhu S; Yong Y; Gu Z; Zhao Y Emerging Strategies of Nanomaterial-Mediated Tumor Radiosensitization. Adv. Mater 2019, 31, 1802244.

(3). Thompson IM; Tangen CM; Paradelo J; Lucia MS; Miller G; Troyer D; Messing E; Forman J; Chin J; Swanson G; Canby-Hagino E; Crawford ED Adjuvant Radiotherapy for Pathologic T3N0M0 Prostate Cancer Significantly Reduces Risk of Metastases and Improves Survival: Long-term Followup of a Randomized Clinical Trial. J. Urol 2009, 181, 956–962. [PubMed: 19167731]

(4). Bolla M; van Poppel H; Collette L; van Cangh P; Vekemans K ; Da Pozzo L; de Reijke TM; Verbaeys A; Bosset J-F; van Velthoven R; Marechal J-M; Scalliet P; Haustermans K; Pierart M Postoperative radiotherapy after radical prostatectomy: a randomised controlled trial (EORTC trial 22911). Lancet 2005, 366, 572–578. [PubMed: 16099293]

(5). Hurwitz MD Chemotherapy and radiation for prostate cancer. Transl. Androl. Urol 2018, 7, 390–398. [PubMed: 30050799]

(6). Goyal S; Kataria T Image guidance in radiation therapy: techniques and applications. Radiol. Res. Pract 2014, 2014, 1–10.

(7). Torresin A; Brambilla MG; Monti AF; Moscato A; Brockmann MA; Schad L; Attenberger UI; Lohr F Review of potential improvements using MRI in the radiotherapy workflow. Z. Med. Phys 2015, 25, 210–220. [PubMed: 25779877]

(8). McPartlin AJ; Li XA; Kershaw LE; Heide U; Kerkmeijer L; Lawton C; Mahmood U; Pos F; van As N; van Herk M; Vesprini D; van der Voort van Zyp J; Tree A; Choudhury A MRI-guided prostate adaptive radiotherapy - A systematic review. Radiother. Oncol 2016, 119, 371–380. [PubMed: 27162159]

(9). Dang A; Kupelian PA; Cao M; Agazaryan N; Kishan AU Image-guided radiotherapy for prostate cancer. Transl. Androl. Urol 2018, 7, 308–320. [PubMed: 30050792]

(10). Beaton L; Bandula S; Gaze MN; Sharma RA How rapid advances in imaging are defining the future of precision radiation oncology. Br. J. Cancer 2019, 120, 779–790. [PubMed: 30911090]

(11). Han Z; Wu X; Roelle S; Chen C; Schiemann WP; Lu ZR Targeted gadofullerene for sensitive magnetic resonance imaging and risk-stratification of breast cancer. Nat. Commun 2017, 8, 692. [PubMed: 28947734]

(12). Penet MF; Krishnamachary B; Chen Z; Jin J; Bhujwalla ZM Molecular imaging of the tumor microenvironment for precision medicine and theranostics. Adv. Cancer Res 2014, 124, 235–256. [PubMed: 25287691]

(13). Zhou Z; Lu ZR Molecular imaging of the tumor microenvironment. Adv. Drug Delivery Rev 2017, 113, 24–48.

(14). Panda A; Obmann VC; Lo WC; Margevicius S; Jiang Y; Schluchter M; Patel IJ; Nakamoto D; Badve C; Griswold MA; Jaeger I; Ponsky LE; Gulani V MR Fingerprinting and ADC Mapping for Characterization of Lesions in the Transition Zone of the Prostate Gland. Radiology 2019, 292, 685–694. [PubMed: 31335285]

(15). Banerjee SR; Ngen EJ; Rotz MW; Kakkad S; Lisok A; Pracitto R; Pullambhatla M; Chen Z; Shah T; Artemov D; Meade TJ; Bhujwalla ZM; Pomper MG Synthesis and Evaluation of Gd(III) -Based Magnetic Resonance Contrast Agents for Molecular Imaging of Prostate-Specific Membrane Antigen. Angew. Chem., Int. Ed 2015, 54, 10778–10782.

(16). Kasivisvanathan V; Rannikko AS; Borghi M; Panebianco V; Mynderse LA; Vaarala MH; Briganti A; Budaus L; Hellawell G; Hindley RG; Roobol MJ; Eggener S; Ghei M; Villers A; Bladou F; Villeirs GM; Virdi J; Boxler S; Robert G; Singh PB; Venderink W; Hadaschik BA; Ruffion A; Hu JC; Margolis D; Crouzet S; Klotz L; Taneja SS; Pinto P; Gill I; Allen C; Giganti F; Freeman A; Morris S; Punwani S; Williams NR; Brew-Graves C; Deeks J; Takwoingi Y; Emberton M; Moore CM MRI-Targeted or Standard Biopsy for Prostate-Cancer Diagnosis. N. Engl. J. Med 2018, 378, 1767–1777. [PubMed: 29552975]

(17). Eberhardt SC Local Staging of Prostate Cancer with MRI: A Need for Standardization. Radiology 2019, 290, 720–721. [PubMed: 30667328]

(18). Krishna S; Lim CS; McInnes MDF; Flood TA; Shabana WM; Lim RS; Schieda N Evaluation of MRI for diagnosis of extraprostatic extension in prostate cancer. J. Magn. Reson. Imaging 2018, 47, 176–185. [PubMed: 28387981]

(19). Pollard JM; Wen Z; Sadagopan R; Wang J; Ibbott GS The future of image-guided radiotherapy will be MR guided. Br. J. Radiol 2017, 90, 20160667. [PubMed: 28256898]

(20). Choi BJ; Jung KO; Graves EE; Pratx G A gold nanoparticle system for the enhancement of radiotherapy and simultaneous monitoring of reactive-oxygen-species formation. Nanotechnology 2018, 29, 504001. [PubMed: 30229748]

(21). Her S; Jaffray DA; Allen C Gold nanoparticles for applications in cancer radiotherapy: Mechanisms and recent advancements. Adv. Drug Delivery Rev 2017, 109, 84–101.

(22). Ni X; Zhang Y; Ribas J; Chowdhury WH; Castanares M; Zhang Z; Laiho M; deWeese TL; Lupold SE Prostate-targeted radiosensitization via aptamer-shRNA chimeras in human tumor xenografts. J. Clin. Invest 2011, 121, 2383–2390. [PubMed: 21555850]

(23). Gandhi N; Wild AT; Chettiar ST; Aziz K; Kato Y; Gajula RP; Williams RD; Cades JA; Annadanam A; Song D; Zhang Y; Hales RK; Herman JM; Armour E; DeWeese TL; Schaeffer EM; Tran PT Novel Hsp90 inhibitor NVP-AUY922 radiosensitizes prostate cancer cells. Cancer Biol. Ther 2013, 14, 347–356. [PubMed: 23358469]

(24). Alcorn S; Walker AJ; Gandhi N; Narang A; Wild AT; Hales RK; Herman JM; Song DY; Deweese TL; Antonarakis ES; Tran PT Molecularly targeted agents as radiosensitizers in cancer therapy–focus on prostate cancer. Int. J. Mol. Sci 2013, 14, 14800–14832. [PubMed: 23863691]

(25). Goswami N; Luo Z; Yuan X; Leong DT; Xie J Engineering gold-based radiosensitizers for cancer radiotherapy. Mater. Horiz 2017, 4, 817–831.

(26). Wang X; Huang SS; Heston WD; Guo H; Wang BC; Basilion JP Development of targeted near-infrared imaging agents for prostate cancer. Mol. Cancer Ther 2014, 13, 2595–2606. [PubMed: 25239933]

(27). Wang X; Tsui B; Ramamurthy G; Zhang P; Meyers J; Kenney ME; Kiechle J; Ponsky L; Basilion JP Theranostic Agents for Photodynamic Therapy of Prostate Cancer by Targeting Prostate-Specific Membrane Antigen. Mol. Cancer Ther 2016, 15, 1834–1844. [PubMed: 27297866]

(28). Luo D; Wang X; Zeng S; Ramamurthy G; Burda C; Basilion JP Targeted Gold Nanocluster-Enhanced Radiotherapy of Prostate Cancer. Small 2019, 15, 1900968.

(29). Miladi I; Alric C; Dufort S; Mowat P; Dutour A; Mandon C; Laurent G; Brauer-Krisch E; Herath N; Coll JL; Dutreix M; Lux F; Bazzi R; Billotey C; Janier M; Perriat P; Le Duc G; Roux S; Tillement O The In Vivo Radiosensitizing Effect of Gold Nanoparticles Based MRI Contrast Agents. Small 2014, 10, 1116–1124. [PubMed: 24659273]

(30). Detappe A; Kunjachan S; Sancey L; Motto-Ros V; Biancur D; Drane P; Guieze R; Makrigiorgos GM; Tillement O; Langer R; Berbeco R Advanced multimodal nanoparticles delay tumor progression with clinical radiation therapy. J. Controlled Release 2016, 238, 103–113.

(31). Kotb S; Detappe A; Lux F; Appaix F; Barbier EL; Tran VL; Plissonneau M; Gehan H; Lefranc F; Rodriguez-Lafrasse C; Verry C; Berbeco R; Tillement O; Sancey L Gadolinium-Based Nanoparticles and Radiation Therapy for Multiple Brain Melanoma Metastases: Proof of Concept before Phase I Trial. Theranostics 2016, 6, 418–427. [PubMed: 26909115]

(32). Detappe A; Thomas E; Tibbitt MW; Kunjachan S; Zavidij O; Parnandi N; Reznichenko E; Lux F; Tillement O; Berbeco R Ultrasmall Silica-Based Bismuth Gadolinium Nanoparticles for Dual Magnetic Resonance-Computed Tomography Image Guided Radiation Therapy. Nano Lett. 2017, 17, 1733–1740. [PubMed: 28145723]

(33). Yu X; Liu X; Wu W; Yang K; Mao R; Ahmad F; Chen X; Li W CT/MRI-Guided Synergistic Radiotherapy and X-ray Inducible Photodynamic Therapy Using Tb-Doped Gd(III)-W-Nanoscintillators. Angew. Chem., Int. Ed 2019, 58, 2017–2022.

(34). Holbrook RJ; Rammohan N; Rotz MW; MacRenaris KW; Preslar AT; Meade TJ Gd(III)-Dithiolane Gold Nanoparticles for T_1-Weighted Magnetic Resonance Imaging of the Pancreas. Nano Lett. 2016, 16, 3202–3209. [PubMed: 27050622]

(35). Brown SD; Nativo P; Smith JA; Stirling D; Edwards PR; Venugopal B; Flint DJ; Plumb JA; Graham D; Wheate NJ Gold Nanoparticles for the Improved Anticancer Drug Delivery of the Active Component of Oxaliplatin. J. Am. Chem. Soc 2010, 132, 4678–4684. [PubMed: 20225865]

(36). Rotz MW; Holbrook RJ; MacRenaris KW; Meade TJ A Markedly Improved Synthetic Approach for the Preparation of Multifunctional Au-DNA Nanoparticle Conjugates Modified with Optical and MR Imaging Probes. Bioconjugate Chem. 2018, 29, 3544–3549.

(37). Vinluan RD 3rd; Yu M; Gannaway M; Sullins J; Xu J; Zheng J Labeling Monomeric Insulin with Renal-Clearable Luminescent Gold Nanoparticles. Bioconjugate Chem. 2015, 26, 2435–2441.

(38). Peng C; Gao X; Xu J; Du B; Ning X; Tang S; Bachoo RM; Yu M; Ge W-P; Zheng J Targeting orthotopic gliomas with renal-clearable luminescent gold nanoparticles. Nano Res. 2017, 10, 1366–1376. [PubMed: 29034063]

(39). Hong S; Leroueil PR; Majoros IJ; Orr BG; Baker JR Jr.; Banaszak Holl MM The binding avidity of a nanoparticle-based multivalent targeted drug delivery platform. Chem. Biol 2007, 14, 107–115. [PubMed: 17254956]

(40). Carney CE; MacRenaris KW; Mastarone DJ; Kasjanski DR; Hung AH; Meade TJ Cell Labeling via Membrane-Anchored Lipophilic MR Contrast Agents. Bioconjugate Chem. 2014, 25, 945–954.

(41). Butterworth KT; McMahon SJ; Currell FJ; Prise KM Physical basis and biological mechanisms of gold nanoparticle radiosensitization. Nanoscale 2012, 4, 4830–4838. [PubMed: 22767423]

(42). Her S; Jaffray DA; Allen C Gold nanoparticles for applications in cancer radiotherapy: Mechanisms and recent advancements. Adv. Drug Delivery Rev 2017, 109, 84–101.

(43). Sancey L; Lux F; Kotb S; Roux S; Dufort S; Bianchi A; Cremillieux Y; Fries P; Coll JL; Rodriguez-Lafrasse C; Janier M; Dutreix M; Barberi-Heyob M; Boschetti F; Denat F; Louis C; Porcel E; Lacombe S; Le Duc G; Deutsch E; Perfettini JL; Detappe A; Verry C; Berbeco R; Butterworth KT; McMahon SJ; Prise KM; Perriat P; Tillement O The use of theranostic gadolinium-based nanoprobes to improve radiotherapy efficacy. Br. J. Radiol 2014, 87 (1041), 20140134. [PubMed: 24990037]

(44). Mangadlao JD; Wang X; McCleese C; Escamilla M; Ramamurthy G; Wang Z; Govande M; Basilion JP; Burda C Prostate-Specific Membrane Antigen Targeted Gold Nanoparticles for Theranostics of Prostate Cancer. ACS Nano 2018, 12, 3714–3725. [PubMed: 29641905]

(45). Runge VM Safety of approved MR contrast media for intravenous injection. J. Magn. Reson. Imaging 2000, 12, 205–213. [PubMed: 10931582]

(46). Yu M; Zheng j. Clearance Pathways and Tumor Targeting of Imaging Nanoparticles. ACS Nano 2015, 9, 6655–6674. [PubMed: 26149184]

(47). Luo D; Wang X; Zeng S; Ramamurthy G; Burda C; Basilion JP Prostate-specific membrane antigen targeted gold nanoparticles for prostate cancer radiotherapy: does size matter for targeted particles? Chem. Sci 2019, 10, 8119–8128. [PubMed: 31588336]

(48). Wang J; Liu G Imaging Nano-Bio Interactions in the Kidney: Toward a Better Understanding of Nanoparticle Clearance. Angew. Chem., Int. Ed 2018, 57, 3008–3010.

(49). Miralbell R; Roberts SA; Zubizarreta E; Hendry JH Dose-fractionation sensitivity of prostate cancer deduced from radiotherapy outcomes of 5,969 patients in seven international institutional datasets: $\alpha/\beta = 1.4$ (0.9–2.2) Gy. Int. J. Radiat. Oncol., Biol., Phys 2012, 82, e17–24. [PubMed: 21324610]

(50). Benjamin LC; Tree AC; Dearnaley DP The role of hypofractionated radiotherapy in prostate cancer. Curr. Oncol. Rep 2017, 19, 30. [PubMed: 28343352]

(51). Yu AC; Badve C; Ponsky LE; Pahwa S; Dastmalchian S; Rogers M; Jiang Y; Margevicius S; Schluchter M; Tabayoyong W; Abouassaly R; McGivney D; Griswold MA; Gulani V Development of a combined MR fingerprinting and diffusion examination for prostate cancer. Radiology 2017, 283, 729–738. [PubMed: 28187264]

(52). Fu G; Zhu L; Yang K; Zhuang R; Xie J; Zhang F Diffusion-Weighted Magnetic Resonance Imaging for Therapy Response Monitoring and Early Treatment Prediction of Photo-thermal Therapy. ACS Appl. Mater. Interfaces 2016, 8, 5137–5147. [PubMed: 26845246]

(53). Ye J; Fu G; Yan X; Liu J; Wang X; Cheng L; Zhang F; Sun PZ; Liu G Noninvasive magnetic resonance/photoacoustic imaging for photothermal therapy response monitoring. Nanoscale 2018,10, 5864–5868. [PubMed: 29560489]

(54). Christiansen RL; Dysager L; Bertelsen AS; Hansen O; Brink C; Bernchou U Accuracy of automatic deformable structure propagation for high-field MRI guided prostate radiotherapy. Radiat. Oncol 2020, 15, 32. [PubMed: 32033574]

(55). Pandit-Taskar N; O'Donoghue JA; Divgi CR; Wills EA; Schwartz L; Gönen M; Smith-Jones P; Bander NH; Scher HI; Larson SM; Morris MJ Indium 111-labeled J591 anti-PSMA antibody for vascular targeted imaging in progressive solid tumors. EJNMMI Res. 2015, 5, 28. [PubMed: 25984435]

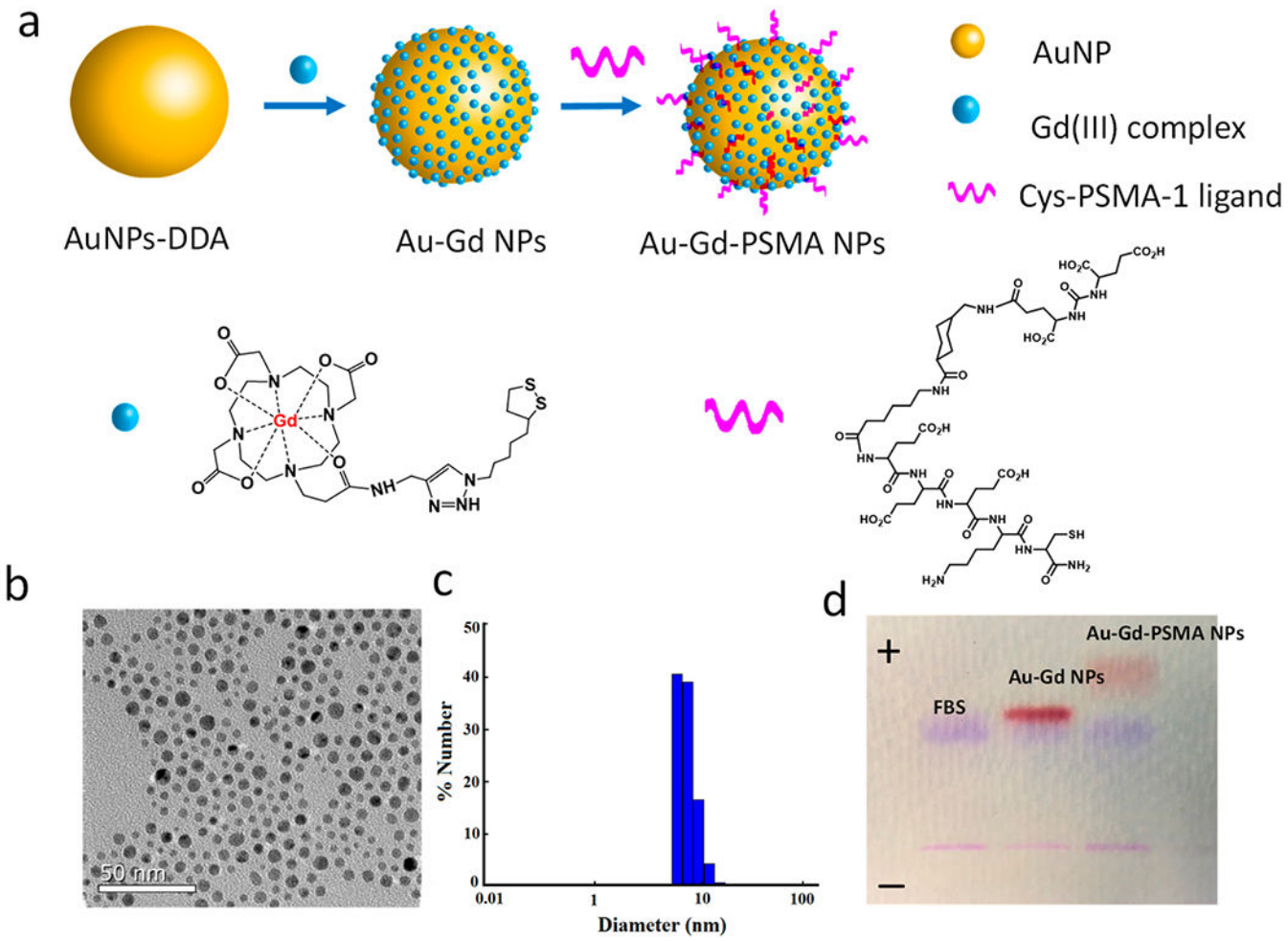

Figure 1.

Au–Gd(III)-PSMA NPs for MR-guided radiation therapy. (a) Schematic representation of Au–Gd(III)-PSMA NPs with AuNPs as the core, Gd(III) complex as the stabilizer on the surface, and Cys-PSMA-1 as the targeting ligand. The Yttrium (Y) complex was synthesized and conjugated to AuNP surfaces as a control. (b) TEM image of Au–Gd(III)-PSMA NPs with an average core size of 5 nm. (c) DLS shows the hydrodynamic diameter of Au–Gd(III)-PSMA NPs. (d) Agarose gel electrophoresis demonstrates the successful binding of Cys-PSMA-1 to AuNPs and stability of Au–Gd(III)-PSMA NPs in serum.

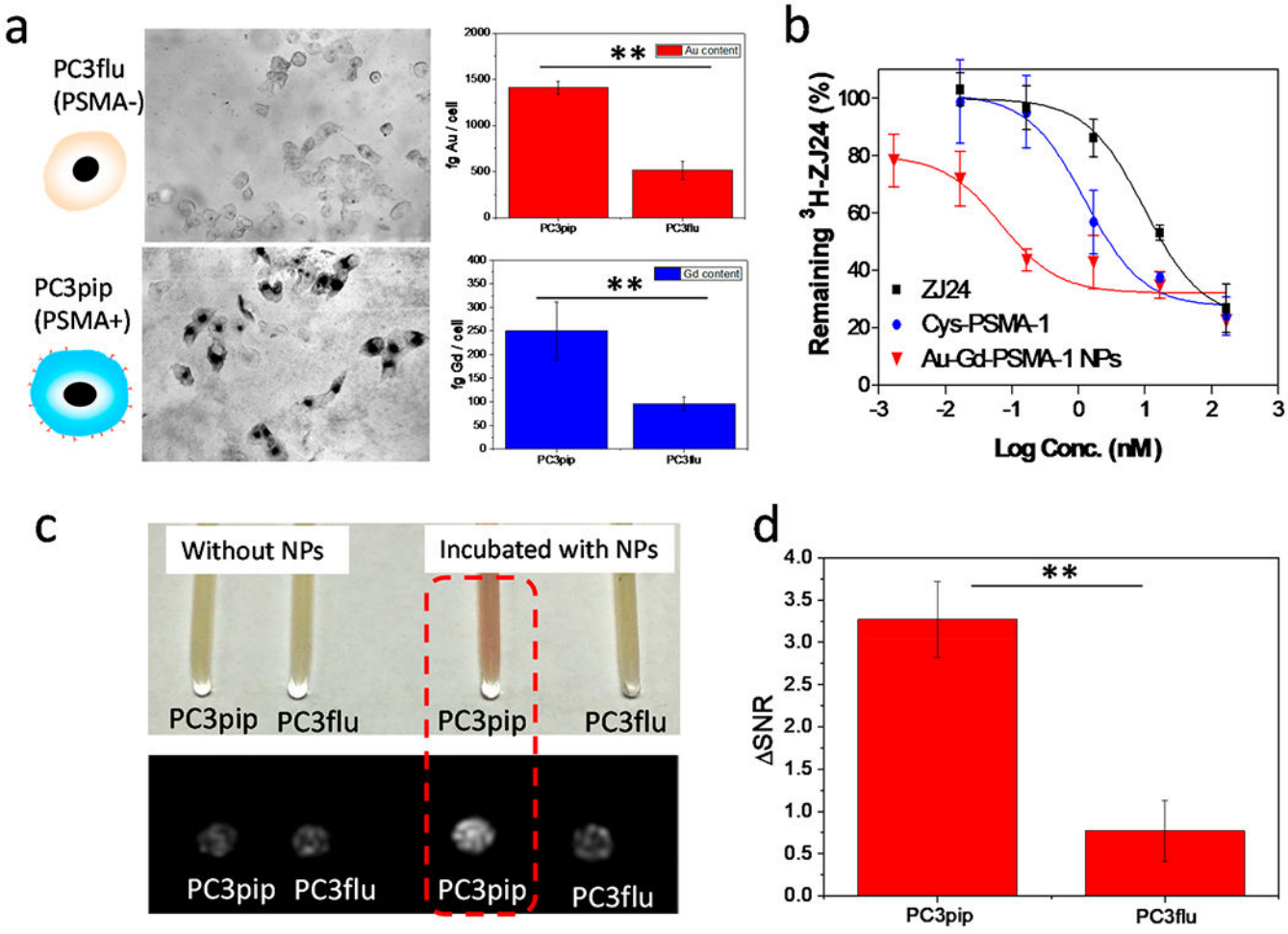

Figure 2.

In vitro cell targeting, binding affinity, and MR contrast. (a) Selective uptake of Au–Gd(III)-PSMA NPs by PC3pip and PC3flu cells. Cells were incubated with NPs for 24 h and then silver stained for visualization. Quantitative Au and Gd(III) content in PC3pip and PC3flu cells was measured with ICP-MS. (b) Competition binding curves for parent ZJ24 ligands, Cys-PSMA-1 ligands, and Au–Gd(III)-PSMA NPs ($n = 3$). (c) Image of PC3pip and PC3flu cell pellets shows NP uptake by PC3pip cells (pink color) and the corresponding T_1-weighted MR images of the cell pellets acquired at 7 T. PC3pip cells incubated with Au–Gd(III)-PSMA NPs demonstrate the highest contrast enhancement. (d) Increased signal-to-noise ratio for PC3pip and PC3flu cells after incubating with Au–Gd(III)-PSMA NPs. Data are presented as the mean ± SD ($n = 3$), and differences between groups are compared with two-tailed *t* tests, $^{**}p \leq 0.01$.

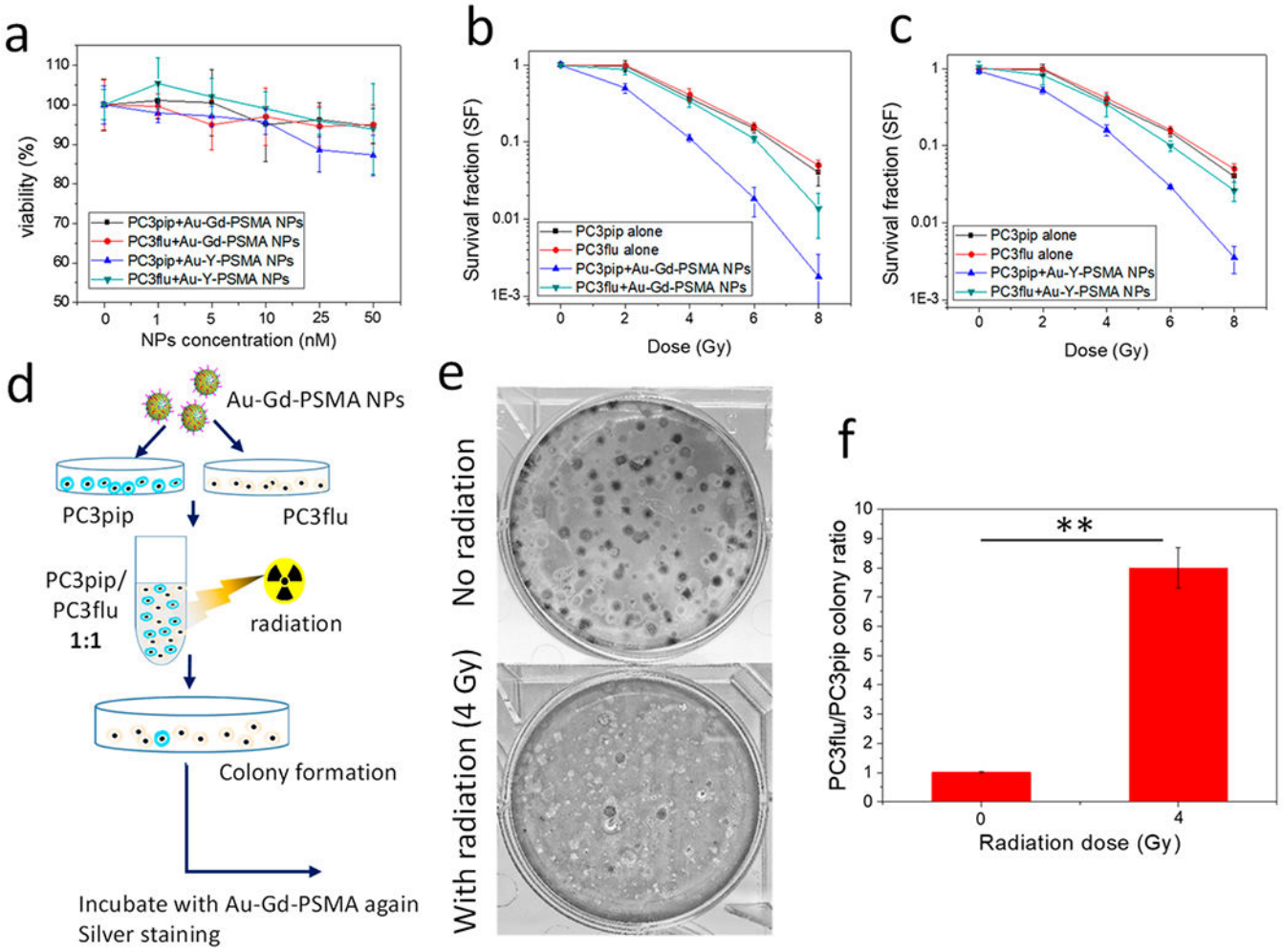

Figure 3.

In vitro radiation enhancement by Au–Gd(III)-PSMA NPs and selective cell killing. (a) Cytotoxicity of Au–Gd(III)-PSMA NPs and Au–Y(III)-PSMA NPs after incubation for 24 h. (b, c) Survival curves of PC3pip and PC3flu cells with and without addition of Au–Gd(III)-PSMA NPs (b) and Au–Y(III)-PSMA NPs (c) at radiation doses of 0, 2, 4, 6, and 8 Gy. (d) Schematic demonstration of selective cell killing experiment with mixed PC3pip and PC3flu colonies. (e) Plates showing mixed colonies stained with silver. PC3pip colonies stained black and PC3flu colonies were relatively transparent. Representative images are shown of $n = 3$. (f) Quantification of the ratio of PC3pip colony number to PC3flu colony number. Data are presented as the mean ± SD ($n = 3$), and differences between groups are compared with two-tailed t tests, $^{**}p \leq 0.01$.

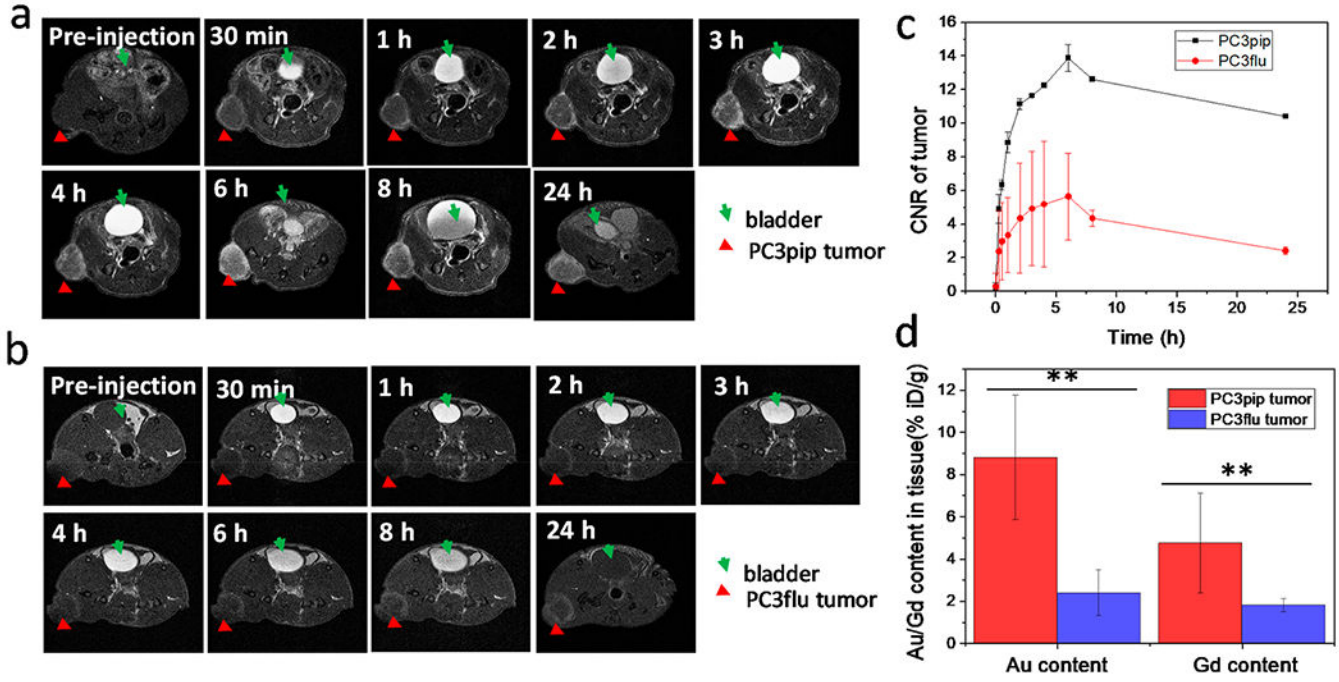

Figure 4.

In vivo tumor targeting of Au–Gd(III)-PSMA NPs and MR imaging. T_1-weighted spin echo images of mice with PC3pip tumor (a) and PC3flu tumor (b) obtained at 7 T. Tumors are indicated by red triangles and bladders are indicated by green arrows. Representative images are shown of $n = 3$. (c) Contrast-to-noise ratio (CNR) of PC3pip and PC3flu tumors relative to muscle, computed from T_1-weighted images ($n = 3$). (d) Au and Gd(III) content in PC3pip and PC3flu tumors 24 h after Au–Gd(III)-PSMA NPs injection. Data are presented as the mean ± SD ($n = 3$), and differences between groups are compared with two-tailed *t* tests, $^{**}p \leq 0.01$.

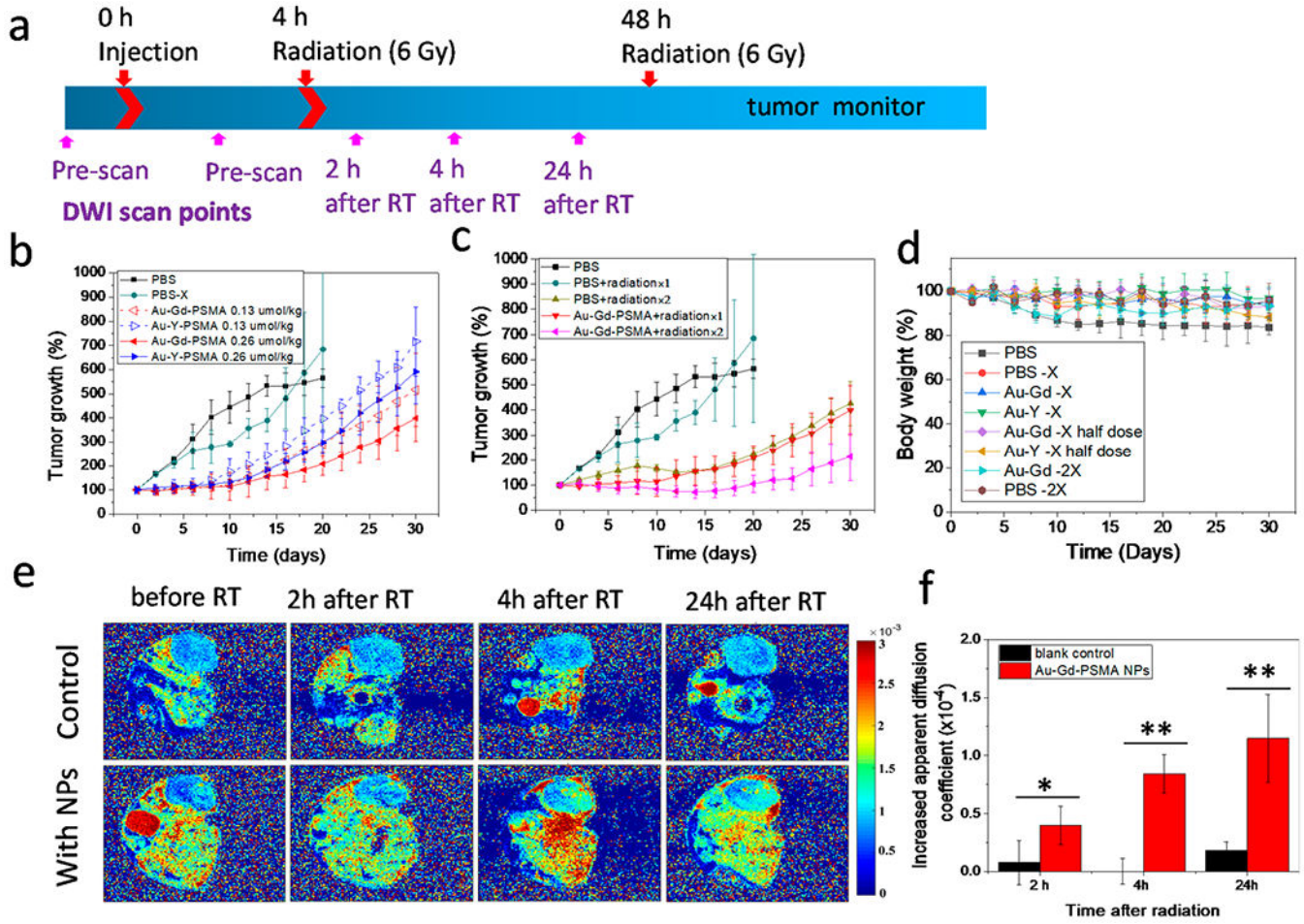

Figure 5.

In vivo Au–Gd(III)-PSMA NP-enhanced radiotherapy. (a) Timeline of Au–Gd(III)-PSMA NPs injection, radiation treatments, and diffusion-weighted imaging (DWI) scanning time points. (b) Tumor growth curves without radiation (PBS) and with one irradiation (6 Gy) after receiving PBS (PBS-X), Au–Gd(III)-PSMA NPs, or Au–Y(III)-PSMA NPs. (c) Tumor growth curves for mice injected with PBS or Au–Gd(III)-PSMA NPs after receiving irradiation (6 Gy) twice. Data are presented as the mean ± SD ($n = 5$). (d) Body weight of mice after each treatment. (e) ADC maps of mice injected with PBS or Au–Gd(III)-PSMA NPs before and at 2, 4, and 24 h after a single irradiation (6 Gy). Representative images are shown of $n = 3$. (f) Increased ADC values at 2, 4, and 24 h after radiation (6 Gy) for mice injected with PBS or Au–Gd(III)-PSMA NPs. Data are presented as the mean ± SD ($n = 3$), and differences between groups are compared with two-tailed *t* tests, $^{*}p \leq 0.05$, $^{**}p \leq 0.01$.

Author Manuscript

Author Manuscript

Author Manuscript

Table 1.

Relaxivities of Gd(III) Complex, Au–Gd(III) NPs, and Au–Gd(III)-PSMA NPs at 1.41 T

	Gd(III) loading per AuNP	r_1 relaxivity (mM^{-1} s^{-1})[a]	
		ionic	particle
Gd(III) complex	NA	5.5	NA
Au–Gd(III)	258 ± 63	32.3	8331
Au–Gd(III)-PSMA	230 ± 10	20.6	4745

[a]"Ionic" r_1 refers to the contribution of each individual Gd(III) complex to proton relaxation, whereas "particle" describes the product of each particle's Gd(III) payload.